



Dust Temperature Uncertainties Hamper the Inference of Dust and Molecular Gas Masses from the Dust Continuum Emission of Quiescent High-redshift Galaxies

R. K. Cochrane¹ , C. C. Hayward¹ , and D. Anglés-Alcázar^{1,2} ¹ Center for Computational Astrophysics, Flatiron Institute, 162 Fifth Avenue, New York, NY 10010, USA; rcochrane@flatironinstitute.org² Department of Physics, University of Connecticut, 196 Auditorium Road, U-3046, Storrs, CT 06269-3046, USA

Received 2022 June 28; revised 2022 August 24; accepted 2022 August 30; published 2022 November 9

Abstract

Single flux density measurements at observed-frame submillimeter and millimeter wavelengths are commonly used to probe dust and gas masses in galaxies. In this Letter, we explore the robustness of this method to infer dust mass, focusing on quiescent galaxies, using a series of controlled experiments on four massive halos from the Feedback in Realistic Environments project. Our starting point is four star-forming central galaxies at seven redshifts between $z = 1.5$ and $z = 4.5$. We generate modified quiescent galaxies that have been quenched for 100 Myr, 500 Myr, or 1 Gyr prior to each of the studied redshifts by reassigning stellar ages. We derive spectral energy distributions for each fiducial and modified galaxy using radiative transfer. We demonstrate that the dust mass inferred is highly dependent on the assumed dust temperature, T_{dust} , which is often unconstrained observationally. Motivated by recent work on quiescent galaxies that assumed $T_{\text{dust}} \sim 25$ K, we show that the ratio between dust mass and 1.3 mm flux density can be higher than inferred by up to an order of magnitude, due to the considerably lower dust temperatures seen in non-star-forming galaxies. This can lead to an underestimation of dust mass (and, when submillimeter flux density is used as a proxy for molecular gas content and gas mass). This underestimation is most severe at higher redshifts, where the observed-frame 1.3 mm flux density probes rest-frame wavelengths far from the Rayleigh–Jeans regime, and hence depends superlinearly on dust temperature. We fit relations between ratios of rest-frame far-infrared flux densities and mass-weighted dust temperature that can be used to constrain dust temperatures from observations and hence derive more reliable dust and molecular gas masses.

Unified Astronomy Thesaurus concepts: [Galaxy evolution \(594\)](#); [Galaxy quenching \(2040\)](#); [Radiative transfer simulations \(1967\)](#); [Submillimeter astronomy \(1647\)](#)

Supporting material: interactive figure, data behind figure

1. Introduction

The gas in galaxies is shaped by complex and connected cycles of physical processes, from the large-scale accretion of cool gas from the cosmic web onto halos, to black hole feeding and the collapse of molecular gas to young stars on small scales, as well as the feedback that ensues from these. Constraining the cosmic gas budget, as a function of gas phase, redshift, and galaxy type, is therefore a key part of understanding the fueling and quenching of star formation in galaxies over time (see Péroux & Howk 2020 for a review).

Since molecular hydrogen (H_2), the direct fuel for star formation, does not have a permanent dipole moment, the mass of molecular gas must be inferred indirectly. In extragalactic studies, this is usually done using measurements of the rotational transitions of carbon monoxide (^{12}CO , hereafter, CO) or the dust continuum emission. Observations of global CO(1–0) line fluxes at low redshift enabled by single-dish facilities such as Arecibo and the IRAM-30 m telescope have enabled constraints on the gas-to-stellar mass fraction (hereafter, simply “gas fraction”) as a function of stellar mass, as well as across the star-formation rate (SFR) stellar mass plane (e.g., Saintonge et al. 2011, 2016, 2017). At higher redshifts, long integration times are required to measure CO(1–0) for a single source, and hence observed samples tend to comprise

massive, submillimeter bright, and/or gravitationally lensed sources (e.g., Danielson et al. 2011; Sharon et al. 2013; Thomson et al. 2015; Sharon et al. 2016). At all redshifts, robust gas masses hinge on a reliable M_{H_2} -to- L_{CO} conversion factor, α_{CO} , which is likely not universal but rather dependent on galaxy properties such as metallicity, gas temperature, and velocity dispersion (see Chiang et al. 2021 and Bolatto et al. 2013 for a review). At high redshifts, brighter higher-order CO transitions are more accessible; these require additional assumptions about the relative luminosities of CO lines (see the review by Carilli & Walter 2013). Despite these significant challenges, very careful analysis has enabled constraints on the evolution of molecular gas to $z \sim 4$ (Decarli et al. 2016, 2019, 2020). These constraints appear to be in qualitative agreement with the evolution of the cosmic star formation history, displaying a decrease of a factor of ~ 6 from $z \sim 1.5$ to the present day.

Use of the dust continuum emission to infer gas mass also has limitations. One method involves sampling the far-infrared (FIR) spectral energy distribution (SED) using multiple bands to derive the dust mass (e.g., Magdis et al. 2012; Dudzeviciute et al. 2020). Inferring the cold gas mass is then subject to uncertainties on the gas-to-dust ratio, which is likely metallicity and redshift dependent (see Rémy-Ruyer et al. 2014; De Vis et al. 2019 and references therein). An alternative is to extrapolate from a single measurement along the Rayleigh–Jeans (R–J) tail (Scoville et al. 2014). Since the R–J tail is nearly always optically thin, with a linear dependence of flux density on dust temperature, the dust mass (and then the gas

mass, again assuming some uncertain conversion; Liang et al. 2018; Privon et al. 2018) may be derived given a dust emissivity per unit mass. This latter method is also dependent on the assumption of a single mass-weighted dust temperature, which is, on average, higher at high redshift (Schreiber et al. 2018; Sommovigo et al. 2022). Empirical scalings between CO-based gas mass and dust luminosity have been derived at low redshift (e.g., Groves et al. 2015 found a linear scaling for the spiral galaxies in the KINGFISH survey; Kennicutt et al. 2011). However, it is not clear that these can be applied at higher redshift (e.g., Decarli et al. 2016 applied the Groves et al. 2015 scaling to galaxies at $z \sim 1$ –2.5 and obtained gas masses ~ 1.5 times lower than CO-derived estimates).

Most studies of interstellar medium (ISM) tracers have been limited to star-forming galaxies. Submillimeter observations of small numbers of individual high- z passive candidates have been performed, generally to confirm that they are indeed quiescent and not highly dust-reddened star-forming sources (e.g., Santini et al. 2019; Kalita et al. 2021; Santini et al. 2021). Since quiescent galaxies tend to be faint at submillimeter wavelengths, population studies are limited to stacking analyses (e.g., Gobat et al. 2018; Magdis et al. 2021), which find considerably larger ISM masses than are observed in quiescent galaxies at $z \sim 0$. Gobat et al. (2018) studied the stacked FIR emission for 977 color-selected quiescent galaxies with $\log_{10}(M_*/M_\odot) > 10.8$ at $1.4 < z < 2.5$ and fitted templates to the stacked dust SED. Their derived dust temperature is 21–25 K, and their derived dust mass is $1_{-0.4}^{+0.6} \times 10^8 M_\odot$. Assuming a gas-to-dust ratio (GDR) of 95, they inferred gas fractions of 5%–10%. Magdis et al. (2021) performed a similar stacking analysis in redshift bins between $z = 2.2$ and $z = 0.3$. They constrained the luminosity-weighted dust temperatures of stacked samples of quiescent galaxies to be $\langle T_{\text{dust}} \rangle = 21 \pm 2$ K, finding little evolution between $z = 2$ and $z = 0$. Assuming a constant solar-metallicity GDR of 92, they derived typical gas fractions for their stacked samples that drop from $\sim 7\%$ to 8% at $z = 2$ to $\sim 2\%$ at $z = 0.5$. There are, however, a number of uncertainties, including the dust-to-gas ratio. Local early-type galaxies may have substantially lower dust-to-gas ratios than local late-type galaxies, so assuming GDRs of ~ 100 may not be valid (Kokusho et al. 2019).

Stacked samples can also suffer contamination. Photometrically selected samples of quiescent galaxies can be contaminated by dusty star-forming galaxies, either due to misclassification of small numbers of sources or from neighboring galaxies via source blending in the lower spatial resolution FIR data. Although observationally expensive, studies of individual galaxies mitigate these risks. Small numbers of existing deep single-source observations present a diverse picture of the gas content of high-redshift quiescent galaxies. Williams et al. (2021) present CO(2-1) observations of six massive ($\log_{10}(M_*/M_\odot) > 11.3$) quiescent galaxies at $z \sim 1.5$, five of which were undetected, and were able to place (3σ) upper limits of gas fractions at 2%–6%. These gas fractions are lower than inferred from the stacking analysis of dust continuum emission presented by Gobat et al. (2018). They are also lower than studies of poststarburst galaxies, which appear to harbor substantial molecular gas reservoirs (though little dense gas; French et al. 2018), despite their low star formation rates (French et al. 2015; Suess et al. 2017; Bezanson et al. 2021).

Expanding samples of individual quiescent galaxies targeted with the Atacama Large Millimeter/submillimeter Array

(ALMA), Whitaker et al. (2021a) presented 1.3 mm observations of six strongly lensed sources from the Resolving Quiescent Magnified (REQUIEM) galaxy survey (Akhshik et al. 2020). The galaxies have redshifts in the range $z = 1.6$ –3.2, and all but one have a very low star formation rate, as derived from ultraviolet-to-near-infrared SED fitting; the highest redshift source has an SFR in line with the main sequence at this redshift. However, Man et al. (2021) find that the SFR derived from SED fitting is higher than that derived from [O II], and argue that this is indicative of recent, rapid quenching. Four of the sources were undetected in the ALMA observations, down to rms values of 9–56 μJy . Whitaker et al. (2021a) follow the methods developed by Scoville et al. (2014), converting limits on $S_{1.3 \text{ mm}}$ to limits on dust mass, assuming a dust temperature of 25 K. Converting this to an upper limit on gas mass using a GDR of 100, they derive upper limits on gas fractions of $\sim 1\%$ for the four undetected sources and argue that these very low gas masses imply rapid early depletion of gas. In a subsequent paper, Whitaker et al. (2021b) caution that their choice of GDR may be inappropriate for the types of galaxies within their sample; in the cosmological hydrodynamical simulation SIMBA (Davé et al. 2019), the GDRs of quiescent galaxies span 6 orders of magnitude.

In this Letter, we investigate a secondary, unstudied aspect: the robustness of inferring the dust mass from $S_{1.3 \text{ mm}}$ for quiescent high-redshift sources. Two linked aspects of this may weaken the robustness of $S_{1.3 \text{ mm}}$ as a dust mass tracer. The first is the impact of a reduction in recent star formation (and hence less dust heating) on the FIR emission of a galaxy. The second potential issue is the fixed observed-frame wavelength; at high redshifts, we probe a shorter rest-frame wavelength and hence move further from the R–J regime, where the flux density depends linearly on temperature. In Section 2, we introduce the hydrodynamical simulations and radiative transfer methods used to create mock SEDs for star-forming and quenched galaxies. In Section 3.1, we infer dust masses for the modeled sources from their 1.3 mm flux densities, assuming a dust temperature of 25 K. In combination with the “ground truth” known from the simulations, we characterize the reliability of these estimates as a function of redshift. In Section 3.2, we show how estimates of a more realistic dust temperature can be made to improve constraints on the dust mass. We draw our conclusions in Section 4.

2. The FIRE Simulations

2.1. Base Simulations of Massive Star-forming Galaxies

Our base simulations are presented in detail in R. K. Cochrane et al. (2022, in preparation), and we provide only a brief summary here. The FIRE project (Hopkins et al. 2014, 2018) is a set of state-of-the-art hydrodynamical cosmological zoom-in simulations that explore the role of stellar feedback in galaxy formation and evolution. In this Letter, we perform controlled experiments on central galaxies of four halos presented by Anglés-Alcázar et al. (2017b), who implemented the FIRE-2 physics model (Hopkins et al. 2018) and a novel on-the-fly treatment for the seeding and growth of super-massive black holes (SMBHs) developed by Anglés-Alcázar et al. (2017a). These halos had originally been simulated by Feldmann et al. (2016, 2017) with the original FIRE model (Hopkins et al. 2014) as part of the MASSIVEFIRE suite. The four halos were selected to have dark matter halo masses of

$M_{\text{halo}} \sim 10^{12.5} M_{\odot}$ at $z = 2$. The central galaxies of these halos have stellar masses of $\sim 7 \times 10^{10} - 3 \times 10^{11} M_{\odot}$ and star formation rates of $\sim 50 - 200 M_{\odot} \text{ yr}^{-1}$ at $z = 2$, with a variety of formation histories; see Feldmann et al. (2017) for details. Note that these simulations do not include feedback from the accreting SMBHs.

For the purposes of illustrating redshift trends in this Letter we focus on a subset of snapshots at $z = 1.5$, $z = 2.0$, $z = 2.5$, $z = 3.0$, $z = 3.5$, $z = 4$, and $z = 4.5$.

2.2. Controlled Quenching Experiments

We perform controlled experiments on the four central galaxies to investigate the impact of quenching star formation on the observable dust continuum emission. For each galaxy at each of the seven redshifts studied, we mimic the quenching of star formation 100 Myr, 500 Myr, or 1 Gyr prior. In practice, this means identifying the stars that formed within the relevant epoch (within $\Delta t_q = [0.1, 0.5, 1]$ Gyr), and replacing their ages with the corresponding value of Δt_q . This is equivalent to assuming that recent stars formed within a single burst. We then predict multiwavelength emission again, following the same methods described in Section 2.3. In each case, we maintain the same galaxy gas and dust content and the same total stellar mass. The only difference between fiducial and modified galaxies is the presence (or absence) of the radiation field of the young stellar populations. We choose not to model these differences within this study; our ‘‘controlled experiment’’ setup is optimized to test the impact of the quenching of recent star formation on the SED most cleanly, without dust mass as an additional varying parameter.

In reality, we expect there to be differences between the gas and dust content of real quiescent and star-forming galaxies. Indeed, the positions of low-redshift galaxies on the stellar-mass star formation rate plane can mostly be explained by their cold gas reservoirs (Saintonge et al. 2016), with specific star formation rate showing a tight correlation with the molecular gas fraction (Spilker et al. 2018). However, as discussed in Section 1, the distribution of gas and dust fractions of quiescent galaxies at high redshift are more poorly constrained. Because of this, and because the aim of this Letter is to test a method rather than put constraints on dust fractions, we do not vary dust mass along with the star formation history. We confirmed that our results are robust to variations in the assumed dust fraction by repeating the experiment with a significantly decreased dust mass (10% of the fiducial value). We discuss this in Section 3.1.

2.3. Synthetic Observations with SKIRT

The primary aim of this Letter is to illustrate the differences in millimeter flux-to-dust mass ratios between high-redshift galaxies that are star-forming and those that are quenched. We first model the observed-frame SEDs for both the fiducial FIRE simulations of star-forming galaxies and our modified quenched galaxies. Following Cochrane et al. (2019), Parsotan et al. (2021), and R. K. Cochrane et al. (2022, in preparation) we use the SKIRT radiative transfer code (Baes et al. 2011; Camps & Baes 2015) to make predictions for the rest-frame ultraviolet-to-far-infrared SEDs of each galaxy snapshot. For both fiducial and modified snapshots, gas and star particles within $0.1 R_{\text{vir}}$ are drawn directly from the FIRE-2 simulation. The only difference is that, for the modified snapshots, stars

formed after the set quenching time are modified within the star particle data file, assuming that they formed in a single burst 100 Myr, 500 Myr, or 1 Gyr prior, and star formation was halted thereafter. The total stellar mass of a modified snapshot is the same as that of its parent star-forming galaxy. We do not alter the gas content of the galaxy or halo, so the gas mass and metallicity of fiducial and modified galaxies are the same, for a given halo and redshift. Dust particles are assumed to follow the distribution of the gas particles, with a dust-to-metals mass ratio of 0.4 (Dwek 1998; James et al. 2002). We assume dust destruction at $>10^6$ K (Draine & Salpeter 1979; Tielens et al. 1994). We model a mixture of graphite, silicate, and polycyclic aromatic hydrocarbon grains using the Weingartner & Draine (2001) Milky Way dust prescription. Star particles are assigned Bruzual & Charlot (2003) SEDs based on their ages and metallicities. We perform the radiative transfer on an octree dust grid, in which cell sizes are adjusted according to the dust density distribution, with the condition that no dust cell may contain more than 0.0001% of the total dust mass of the galaxy.

2.4. The Impact of Controlled Quenching on a Galaxy’s SED

In Figure 1 we present examples of the observed-frame SEDs generated by the radiative transfer modeling for one FIRE galaxy (the central galaxy of halo A8) at two redshifts, $z = 2.0$ (left) and $z = 4.0$ (right). In addition to the SED of the fiducial star-forming galaxy (shown in dark blue), we show the SED predicted for the controlled quenching scenarios (representing, from light blue to dark red, no stars formed within the last 100 Myr, 500 Myr, and 1 Gyr). We also show the ratio between the emission predicted for the controlled quenching scenarios and the fiducial star-forming case (see the lower panels). While we have predicted the observed-frame optical to millimeter emission of the galaxies, in this Letter we focus on the measurable 1.3 mm emission (marked on the SEDs with a dashed vertical line). We choose this wavelength following the recent work of Whitaker et al. (2021a).

For the galaxy snapshot at $z = 1.5$, the effects of quenching star formation on the 1.3 mm emission are modest. There is a small shift in the peak of the dust SED to longer wavelengths, reflecting the colder temperature of the dust due to the softer radiation field in the absence of young massive stars. However, since the observed 1.3 mm emission probes near the R–J tail, the flux density depends approximately linearly on temperature, and so the modest difference in dust temperature does not result in a substantial difference in flux density. At higher redshifts, the observed-frame 1.3 mm flux density probes further from the R–J tail, nearer to the peak of the dust SED; here, modest differences in dust temperature are amplified due to the superlinear dependence of the flux density on temperature. For example, for the $z = 4$ galaxy shown in Figure 1, $S_{1.3 \text{ mm}}$ drops by up to a factor of ~ 5 , despite the dust and gas mass remaining constant by construction. As a result, the ratio of flux density to dust (or gas) mass will vary strongly with dust T , which is sensitive to the recent star formation history. We explore this in Section 3.1.

3. Inferring Dust Mass from Submillimeter Flux Density

3.1. The Robustness of the Dust Mass Inferred from $S_{1.3 \text{ mm}}$

The dust continuum emission of a galaxy is frequently parameterized as follows for the case where the dust is optically thin at the rest-frame frequency (e.g., James et al. 2002;

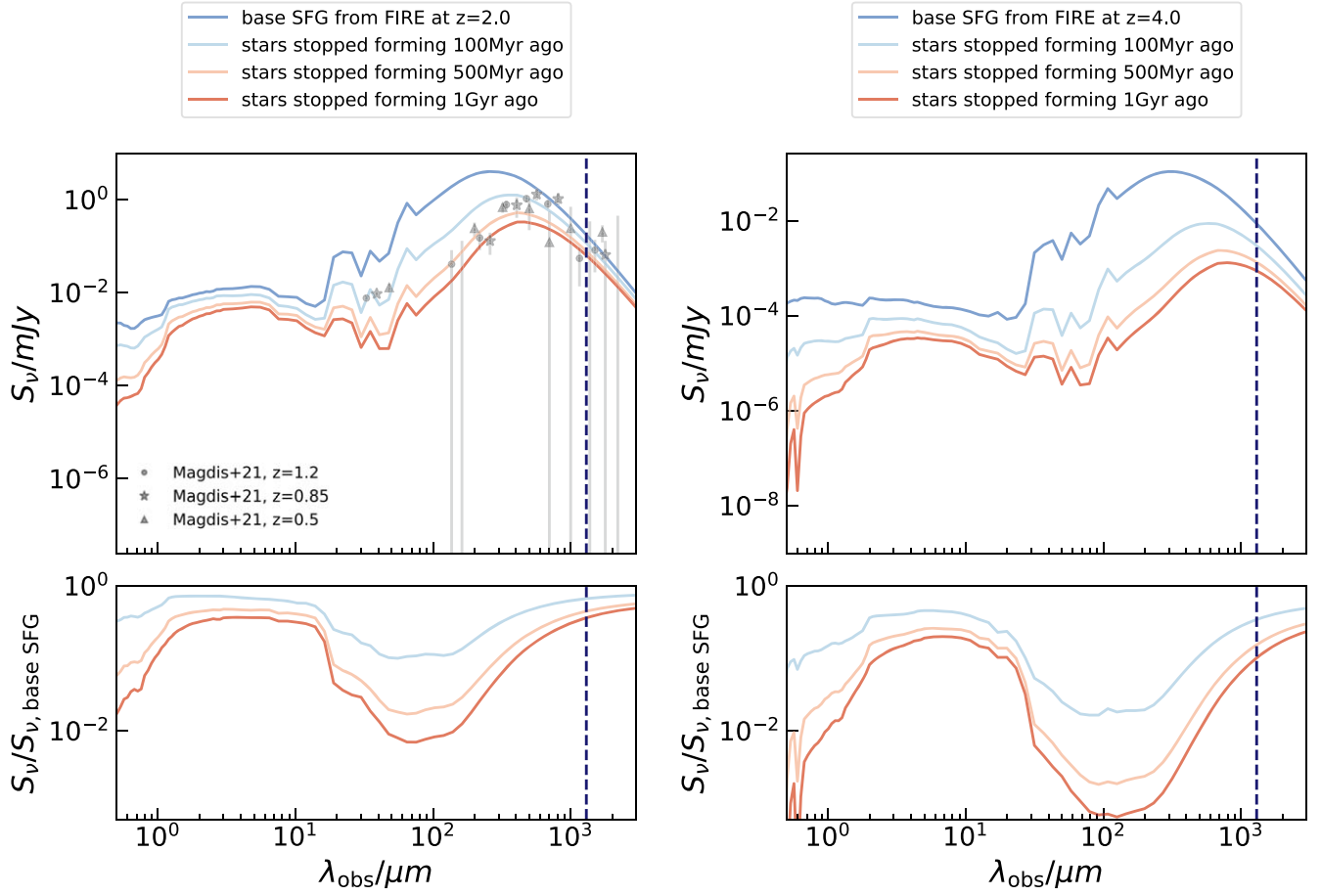


Figure 1. The impact of quenching star formation on a galaxy’s observed-frame SED. Upper panels: dark blue lines show the SED generated for a simulated star-forming galaxy at $z = 2.0$ (left) and $z = 4.0$ (right). Other lines show the impact of a controlled “quenching” event: the pale blue lines show the SED generated if the galaxy had no stars formed within 100 Myr of $z = 2.0$ (or $z = 4.0$); the pale and dark red lines show the same for no stars formed within the prior 500 Myr and 1 Gyr, respectively. We overlay (appropriately redshifted) data from stacked samples of observed color-selected massive quiescent galaxies at $z \sim 0.3\text{--}1.4$ (Magdis et al. 2021) on the panel that shows the SED for the lower-redshift snapshot. The data are in qualitative agreement with our predicted SEDs. Lower panels show the ratio of emission at different wavelengths, relative to the fiducial case of the star-forming source. Dashed navy lines mark an observed-frame wavelength of 1.3 mm. For the quenched galaxies, the radiation field is softer due to the absence of young massive stars and the dust temperature is lower. At $z = 2.0$, 1.3 mm in the observed frame is near the R–J regime, where the flux depends linearly on dust temperature. Hence, the difference in dust temperature between star-forming and quenched sources does not result in a substantial reduction in observed 1.3 mm flux density. At $z = 4$, 1.3 mm probes a shorter rest-frame wavelength (260 μm), and modest temperature differences are amplified because of the superlinear dependence of flux density on dust temperature.

Hayward et al. 2011; Scoville et al. 2017):

$$S_{\nu_{\text{obs}}} = (1 + z) \kappa_{\nu_{\text{rest}}} B_{\nu_{\text{rest}}} (T_{\text{dust}}^{\text{BB}}) \frac{M_{\text{dust}}}{D_L^2}, \quad (1)$$

where $S_{\nu_{\text{obs}}}$ is the observed flux density of the source, z is its redshift, D_L is the corresponding luminosity distance, ν_{rest} is the rest-frame frequency, $B_{\nu_{\text{rest}}}$ is the Planck function, $T_{\text{dust}}^{\text{BB}}$ is the effective dust temperature, and M_{dust} is the total dust mass. $\kappa_{\nu_{\text{rest}}}$ is the dust opacity per unit dust mass (also known as the mass absorption coefficient). This follows a power law in frequency as $\kappa_{\nu_{\text{rest}}} = \kappa_{\nu_{\text{ref}}} \left(\frac{\nu_{\text{rest}}}{\nu_{\text{ref}}}\right)^\beta$, where κ_{ref} is a measured value at some reference frequency, ν_{ref} . We use $\kappa_{\nu_{850\mu\text{m}}} = 0.0484 \text{ m}^2 \text{ kg}^{-1}$ as our reference. We assume a dust emissivity index $\beta = 1.8$, for consistency with Whitaker et al. (2021a).

A simple rearrangement gives the ratio of dust mass to observed flux density:

$$\frac{M_{\text{dust}}}{S_{\nu_{\text{obs}}}} = \frac{1}{1 + z} \frac{D_L^2}{\kappa_{\nu_{\text{rest}}} B_{\nu_{\text{rest}}} (T_{\text{dust}}^{\text{BB}})}. \quad (2)$$

Dust mass can thus be inferred from the observed flux density, and the molecular gas mass is often extrapolated assuming some constant gas-to-dust mass ratio (typically 100, for solar-metallicity gas).

In the R–J regime, $\lambda_{\text{rest}} \gg \frac{hc}{k_B T}$, $B_{\nu_{\text{rest}}} (T_{\text{dust}}^{\text{BB}}) = \frac{2\nu_{\text{rest}}^2 k_B T}{c^2}$, and hence

$$\frac{M_{\text{dust}}}{S_{\nu_{\text{obs}}}} = \frac{D_L^2}{2(1 + z)} \frac{c^2}{\nu_{\text{rest}}^2 k_B T \kappa_{\nu_{\text{rest}}}}. \quad (3)$$

Hence, when in both the optically thin and R–J regimes, $M_{\text{dust}}/S_{\nu} \propto 1/T$.

In this Letter, we explore how the dust-mass-to-flux-density ratio, calculated at an observed wavelength of 1.3 mm (hereafter the “MSR”), changes with redshift and recent star formation history. In the upper panel of Figure 2, we show the MSR for each simulated galaxy, at seven redshifts in the range $z = 1.5$ to $z = 4.5$. Galaxies that have been quenched for longer have lower MSRs, as expected, since the absence of young massive stars causes a softer radiation field and a lower dust temperature. We overplot the expected MSR, calculated

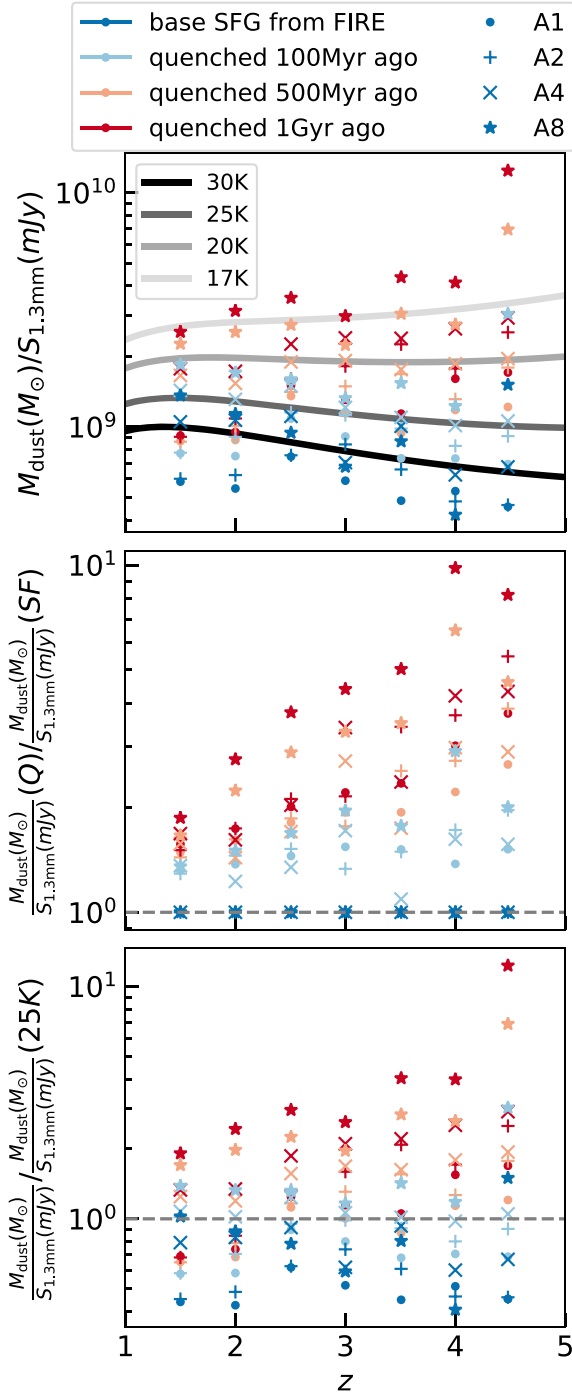


Figure 2. Upper: the M_{dust} -to- $S_{1.3\text{mm}}$ ratio (MSR) derived from our radiative transfer calculations, with predictions for the ratio at different dust temperatures overlaid (see Equation (2)). Middle: the predicted MSR for different quenching scenarios, divided by that calculated for the fiducial star-forming source, for each galaxy at a given redshift. Lower: the calculated MSR divided by the canonical ratio (Equation (2)), assuming a dust temperature of 25 K. For our fiducial sample of star-forming galaxies (dark blue), the true dust mass per unit flux density tends to be slightly lower than predicted, since the mass-weighted dust temperature is actually higher than 25 K. For the quenched galaxies, the true scaling between dust mass and 1.3mm flux density is higher than the canonical ratio by factors of a few. This effect is more pronounced at higher redshifts and can lead to an underestimation of dust (and gas) masses from continuum flux density measurements for galaxies with little or no recent star formation by as much as an order of magnitude.

using Equation (2), for four effective dust temperatures. The fiducial star-forming galaxies tend to have MSRs consistent

with $T_{\text{dust}} \sim 30$ K, while galaxies quenched 500 Myr–1 Gyr prior to the snapshot have MSRs consistent with effective temperatures as low as ~ 17 –20 K. In the middle panel of Figure 2, we quantify the ratio between the MSR of each quenched galaxy and the MSR of the fiducial galaxy at each redshift. This shows the boosting of the MSR relative to the star-forming case. This can be as large as a factor of 10. In the lower panel of Figure 2, we compare the MSR to that expected from Equation (2), assuming a dust temperature of 25 K in line with Scoville et al. (2014, 2017) and the recent work of Whitaker et al. (2021a).

At $z=1.5$ (just lower than the lowest redshift of the Whitaker et al. 2021a sample), the MSR is equal to the expected value to within a factor of ~ 2 . This is expected intuitively from Figure 1: at this redshift, observed-frame 1.3 mm emission probes rest-frame $520 \mu\text{m}$, near to the R–J tail, and is dominated by cool dust in thermal equilibrium. Small deviations from the ratio predicted by Equation (2) will result from different dust temperatures, as $S_\nu/M_{\text{dust}} \propto T$ in the R–J regime (see Equation (3)). As redshift increases, discrepancies between the true MSR and that calculated using Equation (2) become more marked. As shown in the middle panel of Figure 2, the MSR becomes more dependent on temperature with redshift, exceeding that derived, and assuming 25 K by factors of up to 10 at $z > 4$. This is because we have used a fixed observed-frame wavelength, and for our high-redshift quenched sources, we are not probing the R–J tail. For the R–J regime, we require $\lambda_{\text{rest}} \gg \frac{hc}{k_B T}$, i.e., $\lambda_{\text{rest}}/\text{mm} \gg 14.4/T(\text{K})$. For dust temperatures of 25 K, this requires $\lambda_{\text{rest}} \gg 580 \mu\text{m}$, and for temperatures of 20 K, this requires $\lambda_{\text{rest}} \gg 720 \mu\text{m}$. At $z=1.5$, the 1.3 mm flux density probes rest-frame $520 \mu\text{m}$; for R–J, dust temperatures must be $\gg 27.7$ K. At higher redshifts and for lower dust temperatures, the rest-frame wavelength probed by 1.3 mm flux density is far from the R–J regime (see also the right-hand panel of Figure 1), and the flux density depends superlinearly on dust temperature. We demonstrate this in Figure 2; for high-redshift quenched galaxies without a constrained dust temperature, 1.3 mm flux density places weak constraints on the dust (or gas) mass.

To test the robustness of our conclusions to significant changes in dust mass, we repeat the experiment with the dust mass reduced to 10% of the original value. This leads to an increase in the mass-weighted temperature of the dust by several kelvin and a decrease in the amplitude and peak wavelength of the dust SED. However, when we normalize by the dust mass, as we have in this Letter, the difference is very small. Our conclusions are thus insensitive to the exact values of dust mass in high-redshift quiescent galaxies.

Our results are consistent with the observationally driven conclusions of Magdis et al. (2021). They constrain the average luminosity-weighted temperature of color-selected samples of massive ($M_* \sim 10^{11} M_\odot$) quiescent galaxies to be 21 ± 2 K out to $z \sim 2$. They show that following the method presented by Scoville et al. (2017) and assuming a mass-weighted temperature of 25 K leads to an underestimation of gas mass compared to their template-based method. This underestimation factor is ~ 2 –4, in good agreement with the theoretical work presented here.

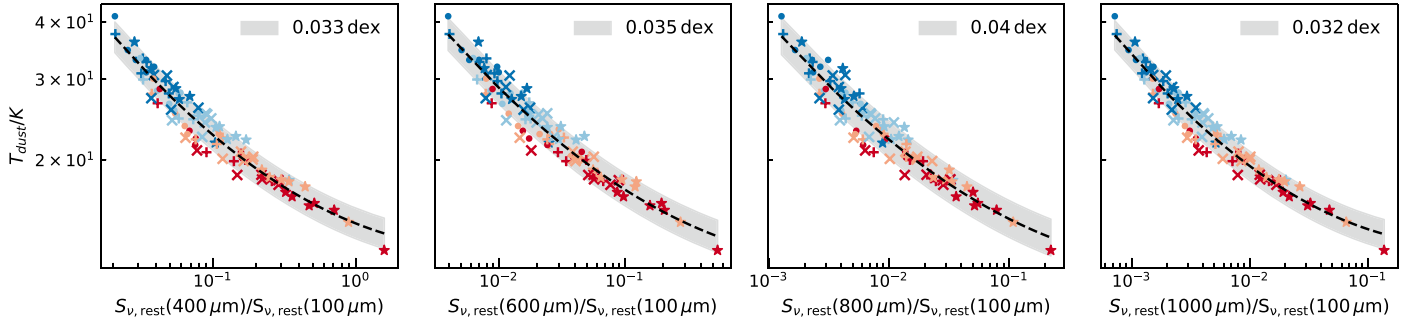


Figure 3. Mass-weighted dust temperature vs. the ratio of two rest-frame flux densities. Colors and symbols are the same as used and defined in Figure 2. The tight correlations show that measurements of two flux densities, or one measurement and an upper limit, can put constraints on the dust temperature, thereby enabling more accurate inference of the dust (and thus the gas) mass. We overplot the best-fitting relations derived for each wavelength combination (black dashed line; see Equation (5)). The shaded region shows the 1σ scatter between the true mass-weighted temperature and the best-fitting relation.

3.2. Constraining the Dust Temperature Using Two Submillimeter Flux Density Measurements

As shown in Section 3.1, the dependence of the submillimeter flux density on the dust temperature causes the MSR to vary depending on the recent star formation history of the galaxy, especially at high redshift. In this section, we show that combining measurements at two rest-frame FIR wavelengths can put constraints on the dust temperature of the galaxy (and hence enable better constraints on the dust mass).³ Far-infrared SEDs of observed galaxies are generally well fitted by a modified blackbody. Assuming this form, the ratio of two rest-frame flux densities, $S_{\nu_{\text{rest},1}}$ and $S_{\nu_{\text{rest},2}}$, is expected to be

$$\frac{S_{\nu_{\text{rest},1}}}{S_{\nu_{\text{rest},2}}} = \frac{(1 - \exp[-\tau_{\nu_{\text{rest},1}}])B_{\nu_{\text{rest},1}}(T_{\text{dust}}^{\text{BB}})}{(1 - \exp[-\tau_{\nu_{\text{rest},2}}])B_{\nu_{\text{rest},2}}(T_{\text{dust}}^{\text{BB}})}, \quad (4)$$

where the optical depth τ_ν is frequently parameterized as $\tau = (\nu/\nu_0)^\beta$ and ν_0 is a constant that relates to the wavelength at which the medium becomes optically thick. In the limit of long wavelengths, $\exp(-\tau_{\nu_{\text{rest}}}) \approx \tau_{\nu_{\text{rest}}}$ and $B_{\nu_{\text{rest}}}(T) \approx \frac{2\nu_{\text{rest}}^2 k_B T}{c^2}$, the ratio of two long wavelength flux densities becomes dependent on the two frequencies and the dust emissivity index, β , alone. When this condition is not satisfied, the flux density ratio also depends on the dust temperature. Here, we consider combinations of rest-frame wavelengths that include one that is firmly outside the R–J regime, to put constraints on the dust temperature. Note that our $S_{\nu_{\text{rest},1}}$ and $S_{\nu_{\text{rest},2}}$ do not include a correction to account for the cosmic microwave background as an observing background. When inferring flux densities from observations, corrections to account for this should be made as usual (see the derivations provided by Da Cunha et al. 2013 and their application in Magdis et al. 2021, for example).

We show the correlation between the mass-weighted dust temperature (calculated directly from the dust grid on which the radiative transfer is performed) and ratios of flux densities at two rest-frame FIR/submillimeter wavelengths (drawn from our modeled SEDs) in Figure 3. Deriving the expected relationship from Equation (4) requires assumptions about β , ν_0 , and the dust temperature distribution. While this can be

³ The effective temperatures inferred from the MSR and the mass-weighted dust temperatures derived directly from the simulations (calculated from the dust grid on which radiative transfer is performed) show excellent agreement. Hence, we focus on constraining the mass-weighted dust temperature here.

performed as required for any choice of these parameters, we present here empirical fits to the data derived from our simulation. These implicitly fold in the dust temperature distribution at different mass-weighted dust temperatures, T_{MW} .⁴ As shown by the dashed black line in each panel of Figure 3, our data are well fitted by a relation of the form:

$$\log_{10}(T_{\text{MW}} [\text{K}]) = q_2 \left(\log_{10} \left(\frac{S_{\nu_{\text{rest},1}}}{S_{\nu_{\text{rest},2}}} \right) \right)^2 + q_1 \log_{10} \left(\frac{S_{\nu_{\text{rest},1}}}{S_{\nu_{\text{rest},2}}} \right) + q_0. \quad (5)$$

We show the fitted coefficients q_2 , q_1 , and q_0 for different combinations of long and short wavelengths in panels (a), (b), and (c) of Figure 4. (see the data used to create this figure for exact numerical values). In panel (d), we show the 1σ scatter in the fitted relation. This was calculated using all snapshots, by comparing the temperature derived from two flux density data points and the relation to the actual mass-weighted dust temperature drawn directly from the simulations. In Figures (a), (b), and (c), we only show combinations of wavelengths for which this scatter is <0.041 dex; this corresponds to the dust temperature being predicted to within 10% of the true value for 68% of snapshots. Given that the relations between combinations of flux densities and the mass-weighted dust temperature are in general so tight we make the coefficients q_2 , q_1 , and q_0 available in the online version of this Letter. We propose that they might be used in observational studies to put constraints on dust temperatures of observed galaxies.

4. Conclusions

In this Letter, we have performed controlled quenching experiments on four simulated massive star-forming galaxies from the FIRE zoom-in simulations at $z = 1.5$ – 4.5 . We study the impact of the cessation of star formation on the galaxies’ SEDs, focusing particularly on the change in observed-frame

⁴ We find that the distribution of dust temperatures within both star-forming and quiescent FIRE galaxies can be well fitted by a normal distribution in $\log_{10}(T [\text{K}])$, i.e., $f(\log_{10}(T)) = \frac{1}{\sigma\sqrt{2\pi}} \exp\left[-\frac{1}{2}\left(\frac{\log_{10}T - \log_{10}T_{\text{MW}}}{\sigma}\right)^2\right]$, with the mean equal to the mass-weighted temperature, T_{MW} , and σ a function of this temperature. Galaxies with higher mass-weighted temperatures tend to have larger values of σ . Fitting σ as a function of T_{MW} yields $\sigma = 0.00327 \times \log_{10}(T_{\text{MW}} [\text{K}]) + 0.00271$.

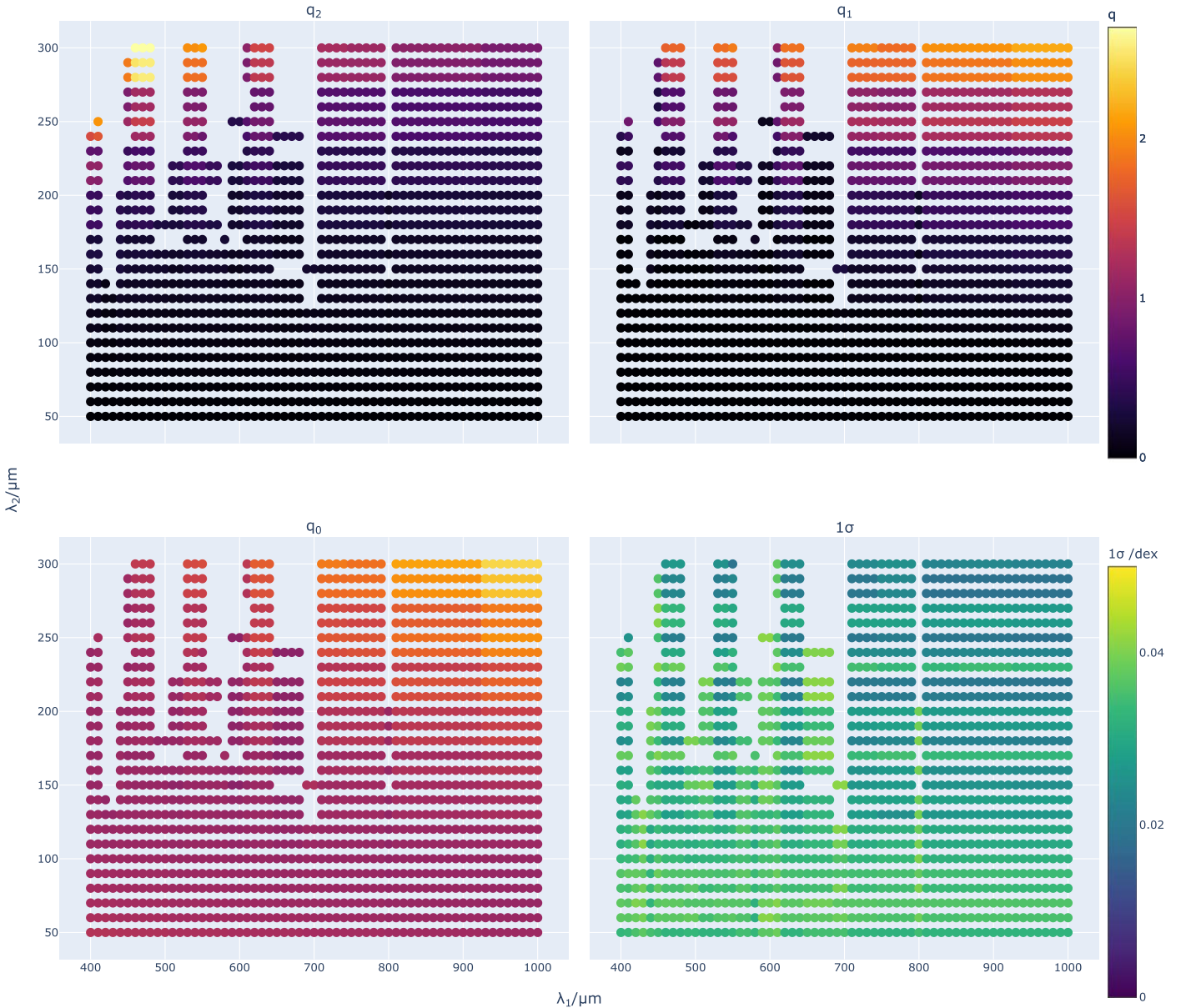


Figure 4. Panels (a), (b), and (c): best-fitting coefficients q_2 , q_1 , and q_0 from Equation (5), fitted using different combinations of rest-frame wavelengths λ_1 and λ_2 . Panel (d) shows the 1σ scatter in the fitted relation, calculated using all snapshots. The scatter characterizes how robustly the mass-weighted temperature can be inferred from the two flux density measurements taken at λ_1 and λ_2 . We only show combinations for which the fitted formula predicts the dust temperature for 68% of snapshots to within 10% (0.041 dex) of the true value. The lowest values of scatter are found for longer wavelengths (i.e., in the upper right-hand corner of the plots). The exact values of the coefficients (available in the data used to create Figure 4) should help constrain dust temperatures of observed galaxies when two submillimeter/millimeter flux densities are available. A plot.ly-based interactive figure is available. The interactive version allows the reader to look up individual values of the coefficients by mousing over the individual scatter plot(s).

(The data used to create this figure are available.)

1.3 mm flux densities. Despite maintaining constant dust mass for the fiducial star-forming and modified quiescent galaxies, the 1.3 mm flux density decreases after quenching by up to an order of magnitude, primarily due to the decrease in dust temperature owing to the absence of young massive stars, which results in a softer radiation field. This effect is particularly strong at high redshifts, where a shorter rest-frame wavelength is probed and 1.3 mm flux density probes far from the R–J regime and depends superlinearly on dust temperature. Our results have implications for observational studies of quenched galaxies, where dust mass is frequently inferred from a single millimeter-wavelength flux density. We highlight the importance of using a realistic dust

temperature in such modeling, and show that an additional measurement at a shorter FIR wavelength can help constrain this. We present fitted relations between mass-weighted dust temperature and ratios of emission at two rest-frame wavelengths that can be applied widely to observational data.

We thank Caleb Choban and Desika Narayanan for helpful comments on an earlier version of this Letter and Rachel Somerville for useful discussions. The Flatiron Institute is supported by the Simons Foundation. D.A.A. was supported in part by NSF grants AST-2009687 and AST-2108944, and CXO grant TM2-23006X.

ORCID iDs

R. K. Cochrane  <https://orcid.org/0000-0001-8855-6107>
 C. C. Hayward  <https://orcid.org/0000-0003-4073-3236>
 D. Anglés-Alcázar  <https://orcid.org/0000-0001-5769-4945>

References

- Akhshik, M., Whitaker, K. E., Brammer, G., et al. 2020, *ApJ*, **900**, 184
 Anglés-Alcázar, D., Davé, R., Faucher-Giguère, C.-A., Özel, F., & Hopkins, P. F. 2017a, *MNRAS*, **464**, 2840
 Anglés-Alcázar, D., Faucher-Giguère, C. A., Quataert, E., et al. 2017b, *MNRAS*, **472**, L109
 Baes, M., Verstappen, J., De Looze, I., et al. 2011, *ApJS*, **196**, 22
 Bezanson, R., Spilker, J. S., Suess, K. A., et al. 2021, *ApJ*, **925**, 153
 Bolatto, A. D., Wolfire, M., & Leroy, A. K. 2013, *ARA&A*, **51**, 207
 Bruzual, G., & Charlot, S. 2003, *MNRAS*, **344**, 1000
 Camps, P., & Baes, M. 2015, *A&C*, **9**, 20
 Carilli, C. L., & Walter, F. 2013, *ARA&A*, **51**, 105
 Chiang, I.-D., Sandstrom, K. M., Chasteney, J., et al. 2021, *ApJ*, **907**, 29
 Cochrane, R. K., Hayward, C. C., Anglés-Alcázar, D., et al. 2019, *MNRAS*, **488**, 1779
 Da Cunha, E., Walter, F., Decarli, R., et al. 2013, *ApJ*, **765**, 9
 Danielson, A. L. R., Swinbank, A. M., Smail, I., et al. 2011, *MNRAS*, **410**, 1687
 Davé, R., Anglés-Alcázar, D., Narayanan, D., et al. 2019, *MNRAS*, **486**, 2827
 De Vis, P., Jones, A., Viaene, S., et al. 2019, *A&A*, **623**, 1
 Decarli, R., Aravena, M., Boogaard, L., et al. 2020, *ApJ*, **902**, 110
 Decarli, R., Walter, F., Aravena, M., et al. 2016, *ApJ*, **833**, 70
 Decarli, R., Walter, F., González-López, J., et al. 2019, *ApJ*, **882**, 138
 Draine, B. T., & Salpeter, E. E. 1979, *ApJ*, **231**, 77
 Dudzeviciute, U., Smail, I., Swinbank, A. M., et al. 2020, *MNRAS*, **494**, 3828
 Dwek, E. 1998, *ApJ*, **1**, 643
 Feldmann, R., Hopkins, P. F., Quataert, E., Faucher-Giguère, C. A., & Kerés, D. 2016, *MNRAS*, **458**, L14
 Feldmann, R., Quataert, E., Hopkins, P. F., Faucher-Giguère, C. A., & Kerés, D. 2017, *MNRAS*, **470**, 1050
 French, K. D., Yang, Y., Zabludoff, A., et al. 2015, *ApJ*, **801**, 1
 French, K. D., Zabludoff, A. I., Yoon, I., et al. 2018, *ApJ*, **861**, 123
 Gobat, R., Daddi, E., Magdis, G., et al. 2018, *NatAs*, **2**, 239
 Groves, B. A., Schinnerer, E., Leroy, A., et al. 2015, *ApJ*, **799**, 96
 Hayward, C. C., Kerés, D., Jonsson, P., et al. 2011, *ApJ*, **743**, 159
 Hopkins, P. F., Kerés, D., Oñorbe, J., et al. 2014, *MNRAS*, **445**, 581
 Hopkins, P. F., Wetzell, A., Kerés, D., et al. 2018, *MNRAS*, **480**, 800
 James, A., Dunne, L., Eales, S., & Edmunds, M. G. 2002, *MNRAS*, **335**, 753
 Kalita, B. S., Daddi, E., D'Eugenio, C., et al. 2021, *ApJ*, **917**, L17
 Kennicutt, R. C., Calzetti, D., Aniano, G., et al. 2011, *PASP*, **123**, 1347
 Kokusho, T., Kaneda, H., Bureau, M., et al. 2019, *A&A*, **622**, A87
 Liang, L., Feldmann, R., Faucher-Giguère, C.-A., et al. 2018, *MNRAS*, **88**, 83
 Magdis, G. E., Daddi, E., Béthermin, M., et al. 2012, *ApJ*, **760**, 6
 Magdis, G. E., Gobat, R., Valentino, F., et al. 2021, *A&A*, **647**, A33
 Man, A. W. S., Zabl, J., Brammer, G. B., et al. 2021, *ApJ*, **919**, 20
 Parsotan, T., Cochrane, R. K., Hayward, C. C., et al. 2021, *MNRAS*, **501**, 1591
 Péroux, C., & Howk, J. C. 2020, *ARA&A*, **58**, 363
 Privon, G. C., Narayanan, D., & Davé, R. 2018, *ApJ*, **867**, 102
 Rémy-Ruyer, A., Madden, S. C., Galliano, F., et al. 2014, *A&A*, **563**, A31
 Saintonge, A., Catinella, B., Cortese, L., et al. 2016, *MNRAS*, **462**, 1749
 Saintonge, A., Catinella, B., Tacconi, L. J., et al. 2017, *ApJS*, **233**, 22
 Saintonge, A., Kauffmann, G., Wang, J., et al. 2011, *MNRAS*, **415**, 61
 Santini, P., Castellano, M., Merlin, E., et al. 2021, *A&A*, **652**, 1
 Santini, P., Merlin, E., Fontana, A., et al. 2019, *MNRAS*, **486**, 560
 Schreiber, C., Elbaz, D., Pannella, M., et al. 2018, *A&A*, **609**, 1
 Scoville, N., Aussel, H., Sheth, K., et al. 2014, *ApJ*, **783**, 84
 Scoville, N., Lee, N., Bout, P. V., et al. 2017, *ApJ*, **837**, 150
 Sharon, C. E., Baker, A. J., Harris, A. I., & Thomson, A. P. 2013, *ApJ*, **765**, 2
 Sharon, C. E., Riechers, D. A., Hodge, J., et al. 2016, *ApJ*, **827**, 1
 Sommovigo, L., Ferrara, A., Pallottini, A., et al. 2022, *MNRAS*, **513**, 3122
 Spilker, J., Bezanson, R., Barišić, I., et al. 2018, *ApJ*, **860**, 103
 Suess, K. A., Bezanson, R., Spilker, J. S., et al. 2017, *ApJL*, **846**, L14
 Thomson, A. P., Ivison, R. J., Owen, F. N., et al. 2015, *MNRAS*, **448**, 1874
 Tielens, A. G. G. M., McKee, C. F., Seab, C. G., & Hollenbach, D. J. 1994, *ApJ*, **431**, 321
 Weingartner, J. C., & Draine, B. T. 2001, *ApJ*, **548**, 296
 Whitaker, K. E., Narayanan, D., Williams, C. C., et al. 2021b, *ApJ*, **922**, L30
 Whitaker, K. E., Williams, C. C., Mowla, L., et al. 2021a, *Natur*, **597**, 485
 Williams, C. C., Spilker, J. S., Whitaker, K. E., et al. 2021, *ApJ*, **908**, 54